Applied Catalysis B: Environmental 158–159 (2014) 391–399

Contents lists available at ScienceDirect

Applied Catalysis B: Environmental

journal homepage: www.elsevier.com/locate/apcatb

# $SiO_2$ promoted $Pt/WO_x/ZrO_2$ catalysts for the selective hydrogenolysis of glycerol to 1,3-propanediol

Shanhui Zhu[a,b,*], Xiaoqing Gao[c], Yulei Zhu[a,c], Jinglei Cui[a,b], Hongyan Zheng[c], Yongwang Li[a,c]

[a] State Key Laboratory of Coal Conversion, Institute of Coal Chemistry, Chinese Academy of Sciences, Taiyuan 030001, PR China
[b] Graduate University of Chinese Academy of Sciences, Beijing 100039, PR China
[c] Synfuels China Co. Ltd., Taiyuan 030032, PR China

ARTICLE INFO

*Article history:*
Received 28 February 2014
Received in revised form 25 April 2014
Accepted 26 April 2014
Available online 4 May 2014

*Keywords:*
Glycerol
Hydrogenolysis
1,3-Propanediol
Pt
$WO_x$

ABSTRACT

To improve 1,3-propanediol selectivity, a series of $SiO_2$ modified $Pt/WO_x/ZrO_2$ catalysts with various $SiO_2$ content for glycerol hydrogenolysis were prepared via deposition–precipitation method followed by sequential impregnation. These catalysts were systematically characterized using BET, ICP, CO chemisorption, XRD, $H_2$-TPR, $NH_3$-TPD, Raman, IR, TEM and XPS. The incorporation of suitable $SiO_2$ into $Pt/WO_x/ZrO_2$ catalysts had extremely favorable effects on the dispersion of $WO_x$ and transformation from crystalline $WO_3$ to active polytungstate, while superfluous $SiO_2$ converted polytungstate to monotungstate. Among them, the 5PtW/ZrSi catalyst reached superior activity and maximum 1,3-propanediol selectivity, up to 52.0%. The structure-activity correlation indicated that glycerol hydrogenolysis conformed to dehydration–hydrogenation reaction mechanism and found that Pt and polytungstate were the most active species.



## 1. Introduction

Renewable resources are attracting more and more attention as alternative raw materials for the synthesis of value-added fuels, chemicals and materials [1,2]. Among them, glycerol has gained considerable interest due to its available production in huge amounts from biodiesel process and capability to produce valued-added products [3]. Nowadays, significant work has been dedicated to the valorization of glycerol by several catalytic processes including dehydration [4], hydrogenolysis [5,6], reforming [7], esterification [8,9] and oxidation [10]. In this context, hydrogenolysis of glycerol to 1,2-propanediol (1,2-PDO) and 1,3-propanediol (1,3-PDO) is considered as a promising approach for their versatile application as important monomer for the production of polyester fibers.

Significant efforts have been focused on glycerol hydrogenolysis to 1,2-PDO, and remarkable advances have been achieved in some literature [11–14]. Our recent work [11] has presented up to 98.0% yield of 1,2-PDO over $B_2O_3$ modified $Cu/SiO_2$ catalyst and found the structure-sensitive feature of glycerol hydrogenolysis. In comparison with 1,2-PDO, 1,3-PDO owns much higher economic value while there are only few reports available on the potential utilization of glycerol for the synthesis of 1,3-PDO. Industrial production of 1,3-PDO is currently on the basis of petroleum route by hydroformylation of ethylene oxide or hydration of acrolein [15]. Nevertheless, selective production 1,3-PDO from biomass-derived glycerol is still a challenge, particularly without high boiling-point organic solvent or acidic additives [16]. It is supposed that the secondary hydroxyl group of glycerol is less accessible to active sites than the primary one because of the steric hindrance effect, which results in low selectivity to 1,3-PDO [17].

It is well-established that crude glycerol from biodiesel process contains water and hydrogenolysis of glycerol leads to an unavoidable accumulation of by-product water, which makes water the preferred solvent in terms of environmental and economic viability. Right now, the relatively effective hydrogenolysis processes using water as solvent mainly employed $Ir–ReO_x/SiO_2$ [18,19] or platinum-based catalysts combined with tungsten species [15,16,20–25]. Tomishige and co-workers [18,19] developed $Ir–ReO_x/SiO_2$ catalyst for glycerol hydrogenolysis using liquid $H_2SO_4$ as co-catalyst; the 1,3-propanediol yield was up to 38%. Nevertheless, the inherent disadvantage of corrosive $H_2SO_4$ greatly hinders to exploit proper reaction technology involving reactor

* Corresponding authors at: State Key Laboratory of Coal Conversion, Institute of Coal Chemistry, Chinese Academy of Sciences, Taiyuan 030001, PR China.
Tel.: +86 351 7117097; fax: +86 351 7560668.
*E-mail addresses:* zhushanhui@sxicc.ac.cn (S. Zhu), zhuyulei@sxicc.ac.cn (Y. Zhu).

http://dx.doi.org/10.1016/j.apcatb.2014.04.049
0926-3373/

and product separation system. Accordingly, alternative heterogeneous solid acid catalyst is highly desirable for practical application. Very recently, we have reported a continuous process for glycerol hydrogenolysis to 1,3-PDO over $ZrO_2$ or $SiO_2$ supported Pt-silicotungstic acid bifunctional catalysts, but these catalysts suffered from deactivation and showed low selectivity [15,24,25]. Kurosaka et al. [16] produced 1,3-PDO by hydrogenolysis of glycerol over $Pt/WO_x/ZrO_2$ catalyst for the first time; the 1,3-PDO yield was up to 24%. However, employing organic solvent 1,3-dimethyl-2-imidazolidinone limited its wide application. Qin et al. [21] exhibited the transformation of glycerol to 1,3-PDO with 45.6% selectivity over $Pt/WO_x/ZrO_2$ catalyst using water as solvent, which provided a sustainable and facile reaction system. To the best of our knowledge, no extensive researches of the $Pt/WO_x/ZrO_2$ catalysts have been reported on the structure-activity relationship for glycerol hydrogenolysis so far. Additionally, the unique role of $WO_x$ species is still not clear for this reaction.

$WO_x/ZrO_2$ or $Pt/WO_x/ZrO_2$ catalysts have been widely investigated and presented excellent reactivity in a variety of reaction processes due to their strong acidity, higher thermal and chemical stability [26–29]. Moreover, a number of additives including $In_2O_3$ [30], Fe [31], $CeO_2$ [32], $CuO_x$ [33] and $Al_2O_3$ [34] have been employed to modify the acidic and electronic properties. Recently, Lauriol-Garbey et al. [4] have communicated that the acrolein selectivity for glycerol dehydration can be improved over $WO_x/ZrO_2$ by doping with $SiO_2$. The addition of $SiO_2$ has marked influence on the textural and acidic properties of $WO_3/ZrO_2$. Appropriate acidity and good dispersion of active metal are indispensable for glycerol hydrogenolysis based on dehydration–hydrogenation bifunctional mechanism, as clarified by our previous reports [24,25]. Nevertheless, no literature have been published regarding structure-performance correlation of $SiO_2$ modified $Pt/WO_x/ZrO_2$ catalysts for glycerol hydrogenolysis. Therefore, the $SiO_2$ modulated $Pt/WO_x/ZrO_2$ as potential catalysts for chemoselective hydrogenolysis of glycerol to 1,3-PDO was explored without using organic solvent. These as-prepared catalysts were fully characterized by various techniques involving BET, ICP, CO chemisorption, XRD, $H_2$-TPR, $NH_3$-TPD, Raman, IR, TEM and XPS. The unique role of $WO_x$ and structure–activity relationship of these $SiO_2$ doped $Pt/WO_x/ZrO_2$ catalysts in glycerol hydrogenolysis was also discussed in detail.

## 2. Experimental

### 2.1. Catalyst preparation

The $SiO_2$ doped $ZrO_2$ samples were prepared by deposition–precipitation method. Firstly, a 0.5 mol/L $Zr(NO_3)_4{\cdot}3H_2O$ (Sinopharm Chemical Reagent Co., Ltd, China (SCRC)) aqueous solution mixed with the desired colloidal silica aqueous solution ($SiO_2$, 30 wt.%, Qingdao Ocean Chemical CO., Ltd, China) under vigorous stirring. Then, a 28 wt.% ammonia (SCRC) aqueous solution was dripped into it at 80 °C until the pH was attained to 9. The mixture was aged at 80 °C for 2 h, filtrated and washed with hot deionized water for 5 times. Finally, these precipitate was dried at 110 °C overnight and then calcined at 600 °C in static air for 4 h.

These $SiO_2$ doped $ZrO_2$ samples were impregnated with an aqueous solution containing the desired amount of ammonium paratungstate (SCRC). After impregnation, these samples were dried overnight at 110 °C and then calcined at 600 °C in static air for 4 h. The above samples were further impregnated with an aqueous solution of $H_2PtCl_6{\cdot}6H_2O$ (SCRC). Impregnated samples were dried overnight at 110 °C and then calcined in static air at 400 °C for 4 h. The obtained catalysts are designated as *x*PtW/ZrSi, where the *x* (wt.%) represents $SiO_2$ nominal mass loading in the $SiO_2$-$ZrO_2$ mixed support. In all catalysts the nominal weight loading of Pt and $WO_x$ (quantified in the form of $WO_3$) were fixed at 2 wt.% and 15 wt.%, respectively.

### 2.2. Catalyst characterization

$N_2$ adsorption–desorption isotherms were performed at −196 °C on a Micromeritics ASAP 2420 instrument. These samples were first degassed under vacuum at 300 °C for 8 h.

ICP optimal emission spectroscopy (Optima2100DV, PerkinElmer) was employed to determine the compositions of as-prepared catalysts.

Powder X-ray diffraction (XRD) patterns were carried out on a D2/max-RA X-ray diffractometer (Bruker, Germany) with Cu *K*α radiation. The X-ray patterns were measured in $2\theta$ values in the range from 10° to 90° at a 5° $min^{-1}$ scan speed.

CO chemisorption was conducted in Auto Chem.II2920 equipment (Mircromeritics, USA). For each run, 0.2 g catalyst sample was placed in a quartz tube and reduced in $H_2$ for 2 h at 200 °C. After that, the sample was flushed with He for 1 h, cooled down to 50 °C and then pulse injected pure CO. The Pt dispersion was determined by assuming that the stoichiometry of adsorbed CO molecule to surface platinum atom was one.

Temperature-programmed reduction of hydrogen ($H_2$-TPR) was carried out in the same apparatus as above. For each run, about 0.1 g sample was placed into a *U*-shaped quartz tube and pretreated in Ar at 300 °C for 30 min and then cooled to 50 °C. After that, a 10 vol% $H_2$–Ar mixed gas was employed and a cold trap with isopropanol–liquid nitrogen slurry was used to condense the water vapor. The $H_2$-TPR was started from 50 °C to 1000 °C at a ramp of 5 °C/min and simultaneously monitored by a thermal conductivity detector (TCD).

Temperature-programmed desorption of ammonia ($NH_3$-TPD) was performed in the same apparatus as CO chemisorption. At first, 0.3 g catalyst sample was pretreated in He at 400 °C for 1 h and then cooled to 100 °C followed by saturating with pure $NH_3$ for 30 min. Subsequently, the sample was heated to 700 °C at a rate of 5 °C/min and the desorbed $NH_3$ was monitored with a MS (Agilent, USA).

Raman spectroscopy was recorded on a LabRAM HR800 System using a CCD detector at room temperature. The 325 nm of the He–Cd laser was employed as the exciting source with a power of 30 MW.

FTIR spectra were conducted on a Vertex 70 (Bruker) FT-IR spectrophotometer with a deuterium triglycine sulfate (DTGS) detector. The powder samples were mixed with KBr (2 wt.%) and pressed into translucent disks at room temperature.

TEM measurement was carried out on a field-emission transmission electron microscopy (FETEM, JEM-2011F) operating at 200 kV voltages. The reduced samples were suspended in ethanol with an ultrasonic dispersion for 30 min and deposited on carbon-coated copper grids.

X-ray photoelectron spectroscopy (XPS) were performed on a VG MiltiLab 2000 spectrometer with Mg *K*α radiation and a multichannel detector. Prior to each test, the calcined sample was reduced in $H_2$ at 200 °C for 2 h. The binding energies were referenced using the C1s peak at 284.6 eV. The experiment error was given within ±0.1 eV.

### 2.3. Catalytic reaction

Glycerol hydrogenolysis tests were conducted in a vertical fixed-bed stainless steel reactor (12 mm of inner diameter, length of 600 mm). Typically, 3.0 g catalyst (20–40 mesh) was loaded in the constant temperature section of the reactor with quartz sand packed in both ends. Prior to the reaction, the sample was prereduced in flowing $H_2$ (100 mL/min) at 200 °C for 2 h. Subsequently,

**Table 1**
Physicochemical properties and acidities of different catalysts.

| Catalyst | $S_{BET}$ ($m^2$/g) | $D_{pore}$ (nm) | $V_{pore}$ ($cm^3$/g) | Pt size (nm) | Pt dispersion (%) | Total acidity (mmol $NH_3$/g) |
|---|---|---|---|---|---|---|
| PtW/Zr | 35.1 | 6.1 | 0.071 | 4.8 | 23.4 | 0.25 |
| 2.5PtW/ZrSi | 101.2 | 3.6 | 0.104 | 3.2 | 35.5 | 0.35 |
| 5PtW/ZrSi | 113.3 | 3.5 | 0.121 | 2.7 | 41.3 | 0.38 |
| 7.5PtW/ZrSi | 121.2 | 4.0 | 0.128 | 3.0 | 37.4 | 0.36 |
| 10PtW/ZrSi | 152.4 | 3.7 | 0.154 | 3.4 | 33.8 | 0.34 |

a 10 wt.% glycerol aqueous solution (3.0 g/h) with flowing $H_2$ (100 mL/min) were continuously pumped into the reactor inlet by an HPLC pump. The liquid and gas products were condensed and collected in a gas–liquid separator immersed in an ice–water trap. The standard reaction conditions were listed as follows: 180 °C, 5.0 MPa, $H_2$/glycerol/$H_2O$ = 82:1:46 (molar ratio), weight hourly space velocity (WHSV) = 1.0 g/$g_{cat}$/h, in which the WHSV was defined as the grams of feed per gram of catalyst and per hour.

The liquid products were analyzed by an off-line gas chromatography (Ruihong chromatogram analysis Co., Ltd, China) using a FID detector and a DB-WAX capillary column. The outlet gas was on-line analyzed by a gas chromatograph (Agilent 6890N, USA) equipped with a TCD detector. The obtained products were identified by GC–MS (6890N/5973MSD, Agilent, USA).

Generally, the carbon balances accounted for 92–105% during the steady state. The identified products were 1,3-PDO, 1,2-PDO, 1-propanol (1-PO), 2-propanol (2-PO), ethanol, acetol, propionic acid, acetic acid, ethylene glycol, methanol, propane, methane and $CO_2$. The conversion of glycerol and selectivity of products were calculated using the following expressions:

$$\text{conversion}(\%) = \frac{\text{moles of glycerol (in)} - \text{moles of glycerol (out)}}{\text{moles of glycerol (in)}} \times 100$$

$$\text{selectivity}(\%) = \frac{\text{moles of one product}}{\text{moles of all products}} \times 100$$

## 3. Results

### 3.1. Catalyst characterization

#### 3.1.1. Physicochemical properties of catalysts

Table 1 displays the textural properties originated from nitrogen physisorption isotherms of as-prepared catalysts. For the $SiO_2$-free catalyst, the BET surface area was only 35.1 $m^2$/g. In comparison, with the promotion of $SiO_2$, even in a minor amount, the BET surface area increased remarkably. For example, the BET surface area was up to 101.2 $m^2$/g over 2.5PtW/ZrSi catalyst. It can be observed that the BET surface area improved from 35.1 to 152.4 $m^2$/g while the pore volume also increased moderately with an increase in $SiO_2$ amount. This result indicated that the doping of $SiO_2$ enhanced BET surface area and formed large amounts of mesoporous pores during the preparation procedure, consistent well with the previous reports [4,35]. As described in Table S1, the element contents determined by ICP were close to nominal values. The CO chemisorption on the reduced catalysts was used to estimate Pt particle size and dispersion. As compiled in Table 1, the incorporation of $SiO_2$ decreased Pt particle size notably and simultaneously improved Pt dispersion significantly. Similar trend has been observed in the case of $SiO_2$ modified Rh/$ZrO_2$ catalyst [36].

The XRD patterns of PtW/ZrSi catalysts are shown in Fig. 1. For the $SiO_2$-free PtW/Zr catalyst, the XRD patterns mainly displayed diffraction peaks corresponding to monoclinic $ZrO_2$ at $2\theta$ = 24.1°, 28.3°, 31.5°, 34.3° and 49.4°, and small amount of tetragonal $ZrO_2$ was observed at $2\theta$ = 30.17° [37]. Interestingly, the XRD diffraction peaks of monoclinic $ZrO_2$ disappeared while the tetragonal $ZrO_2$ at $2\theta$ = 30.17° was remained as the only $ZrO_2$ crystalline phase due to $SiO_2$ doping, inferring that $SiO_2$ can facilitate to stabilize metastable tetragonal $ZrO_2$. With the increasing $SiO_2$ content, the intensity of diffraction peaks for tetragonal $ZrO_2$ declined remarkably, and the peak width broadened gradually. When the $SiO_2$ content increased to 10 wt.%, only amorphous $ZrO_2$ was detected [4]. The combined results suggested that the incorporation of minor $SiO_2$ promoted the formation of tetragonal $ZrO_2$ while too much $SiO_2$ led to generate amorphous $ZrO_2$. The $SiO_2$ free-PtW/Zr sample exhibited obvious diffraction peaks of monoclinic $WO_3$ at $2\theta$ = 23.2°, 23.7°, 24.3° and 30.2° [27]. However, only extremely traces of monoclinic $WO_3$ were detected for $SiO_2$-comtaining samples, most probably because $SiO_2$ doping boosted homogeneous dispersion of $WO_3$ species on the surface. Meanwhile, no XRD diffraction peak showed any evidence of Pt nanoparticles, suggesting that these Pt nanoparticles were highly dispersed on support surface, in well agreement with the CO chemisorption results.

The Raman spectra of PtW/Zr catalysts with and without $SiO_2$ dopants are displayed in Fig. 2. The PtW/Zr sample showed typical bands for monoclinic $ZrO_2$ at 349, 380, 561 and 617 $cm^{-1}$ as well as the bands at 320, 476 and 644 $cm^{-1}$ ascribed to tetragonal $ZrO_2$ [33]. The $SiO_2$ modified catalysts exhibited only the bands for tetragonal $ZrO_2$, consistent well with the XRD results. The Raman bands centered at 274, 715 and 808 $cm^{-1}$ were assigned to characteristic bands of m-$WO_3$ phase [31]. Moreover, the intensity of these bands decreased significantly with the increasing $SiO_2$ content, reflecting that the incorporation of $SiO_2$ essentially suppressed the growing of $WO_3$ domain size on the zirconia surface and improved the dispersion of $WO_x$ species, most probably due to the enhanced interaction. A band centered at 973 $cm^{-1}$ was associated with the stretch mode of monooxo W=O species corresponding to highly

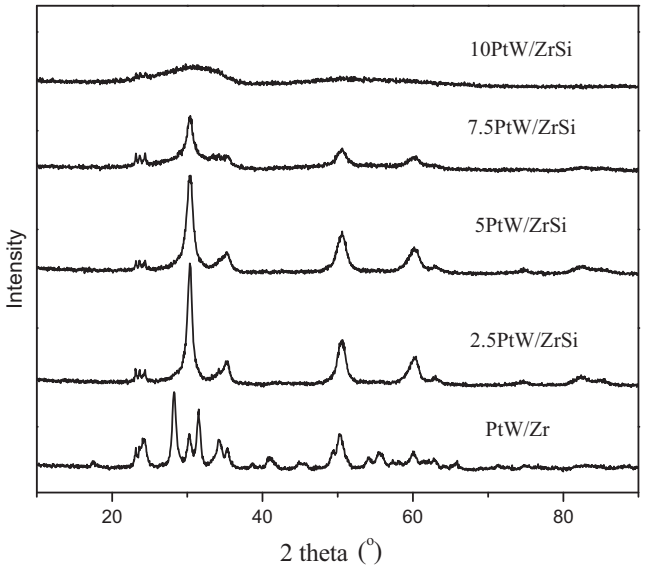


**Fig. 1.** XRD patterns of $SiO_2$ modified PtW/Zr catalysts.

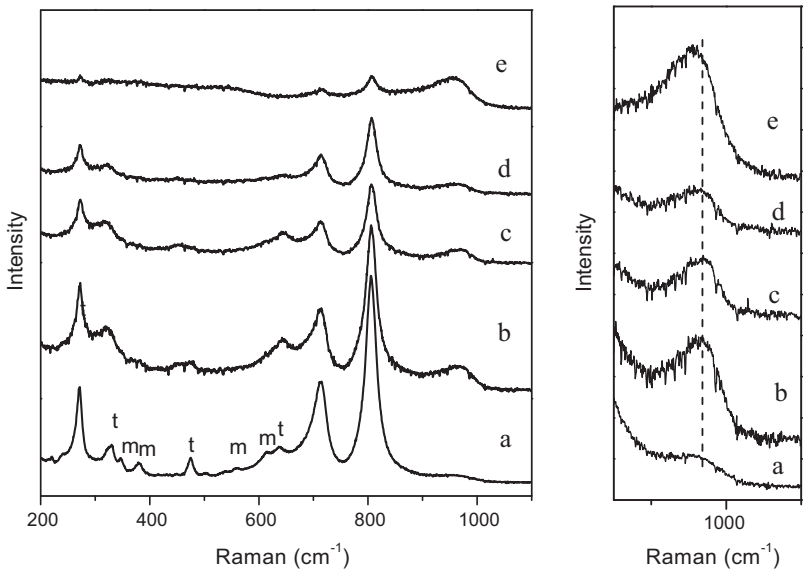


**Fig. 2.** Raman spectra of calcined (a) PtW/Zr, (b) 2.5PtW/ZrSi, (c) 5PtW/ZrSi, (d) 7.5PtW/ZrSi and (e) 10PtW/ZrSi.

dispersed $WO_x$ species [34]. Meanwhile, this band shifted gradually from 973 $cm^{-1}$ to 956 $cm^{-1}$ with the increasing $SiO_2$ content, revealing that the polytungstate species gradually transformed into isolated monotungstate species [27,34].

Fig. 3 illustrates the IR spectra for the $SiO_2$ doped PtW/Zr catalysts in the range of 600–2000 $cm^{-1}$. The bands at 744 $cm^{-1}$ and 1625 $cm^{-1}$ were ascribed to the various vibration modes of surface Zr—OH bonds [38]. It can be observed that a new band emerged at 808 $cm^{-1}$ corresponding to Si—O—Si symmetric bond while the band at 1630 $cm^{-1}$ was attributed to the Si—OH stretching of terminal silanol [11]. The $SiO_2$ doping induced another new weak bands centered at 972 $cm^{-1}$ and 1045 $cm^{-1}$, which was ascribed to Si—O—Zr linkages and asymmetric stretching vibration of Si—O—Si bonds, respectively [39]. It should be noted that both two bands underwent obvious shift towards lower wavenumbers and intensified with the increasing $SiO_2$ amount. Specifically, the band of Si—O—Zr linkages ranged from 972 $cm^{-1}$ for 2.5PtW/ZrSi to 940 $cm^{-1}$ for 10PtW/ZrSi, while the band of Si—O—Si bond shifted from 1045 $cm^{-1}$ to 1020 $cm^{-1}$. The red shift of Si—O—Si bond band was related to the deteriorating silica framework after insertion of Zr atom [39,40]. During the preparation process, $Zr^{4+}$ and $SiO_2$ sol were mixed and precipitated together; the formation of zirconium oxyhydroxide would be surrounded by $SiO_2$. The close contact between $SiO_2$ and $ZrO_2$ resulted in the formation of strong interaction and presence of Si—O—Zr linkages in the composite materials.

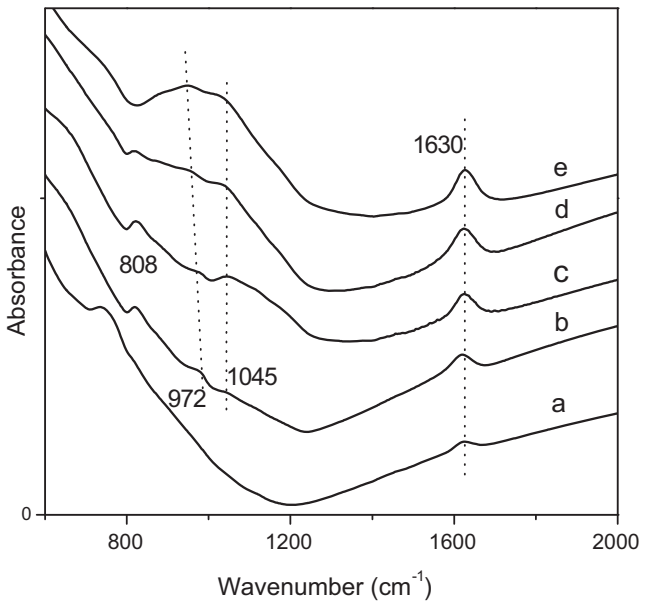


**Fig. 3.** FTIR spectra of calcined (a) PtW/Zr, (b) 2.5PtW/ZrSi, (c) 5PtW/ZrSi, (d) 7.5PtW/ZrSi and (e) 10PtW/ZrSi.

TEM and HRTEM images of representative PtW/Zr and 5PtW/ZrSi catalysts are illustrated in Fig. 4. The Pt nanoparticles in the PtW/Zr sample did not occur obvious agglomeration and the average particle diameter was 3.6 nm, despite some larger particles (>5 nm). When suitable $SiO_2$ was incorporated into this sample, the average particle diameter obviously decreased to 2.3 nm and no particles larger than 5 nm were observed. Moreover, 88% of Pt nanoparticles were in the range of 1.5–3.5 nm, suggesting that these Pt nanoparticles exhibited homogeneous distribution and did not show any evidence of agglomeration over 5PtW/ZrSi. The HRTEM images of PtW/Zr mainly exhibited m-$ZrO_2$ structure with d-spacing 0.29 nm [27]. Large amounts of $ZrO_2$ stabilized m-$WO_3$ clusters can be clearly confirmed by lattice fringes ($d$ = 0.36 nm) over PtW/Zr [27]. However, almost no obvious m-$WO_3$ clusters were detected over 5PtW/ZrSi. Similarly, the signature resonances for well-ordered crystalline $WO_3$ nanoparticles were absent in XRD measurements. The above fact confirmed that primarily TEM-invisible monotungstate and polytungstate species existed in the 5PtW/ZrSi sample.

### 3.1.2. *Reducibility and surface acidic properties of catalysts*

$H_2$-TPR has been applied widely to obtain semi-quantitative results of domain sizes and monolayer capacities for surface oxides. Generally, highly dispersed metal oxides tend to reduce at higher temperature than bulk ones due to the strong interaction with oxide support. As shown in Fig. 5, the peaks corresponding to $PtO_x$ reduction between 50 °C and 250 °C were observed in all cases. In this region, the $SiO_2$-free PtW/Zr sample presented a reduction peak at 85 °C. This peak shifted toward higher temperature with the increasing $SiO_2$ loading, most probably due to the increased interaction between Pt and $SiO_2$–$ZrO_2$ mixed support. Interestingly, a weak band centered at 190 °C was observed over 2.5PtW/ZrSi and 5PtW/ZrSi, which may result from hydrogen spillover [41]. Based on Barton et al.'s report [42], the reduction profiles of $WO_3$

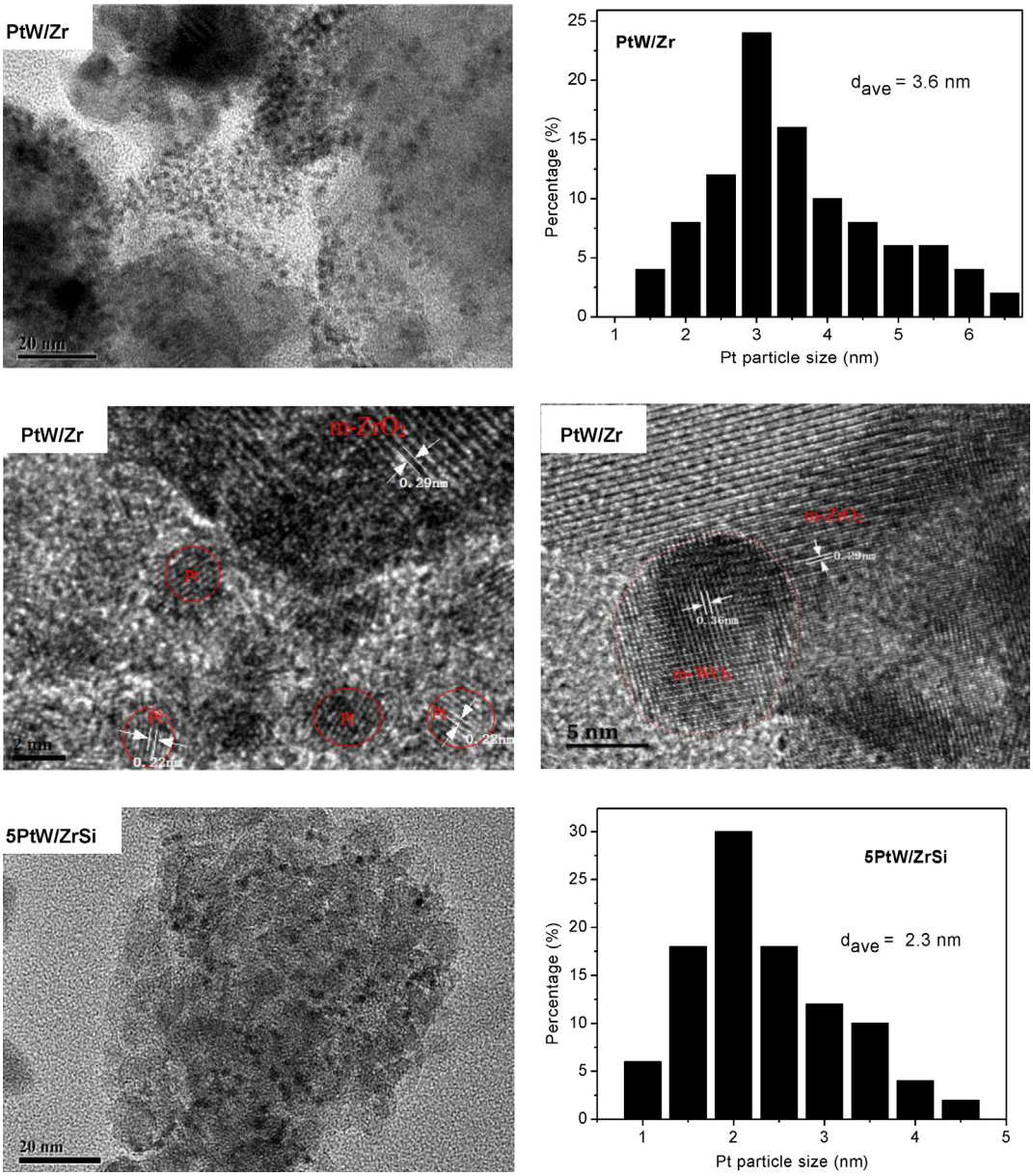


**Fig. 4.** TEM and HRTEM images of reduced PtW/Zr and 5PtW/ZrSi catalysts with Pt particle size distribution.

species were very broad and contained four overlapping peaks. The first three peaks were ascribed to the following successive stages: $WO_3 \rightarrow WO_{2.9}$ (300–500 °C), $WO_{2.9} \rightarrow WO_2$ (550–700 °C) and $WO_2 \rightarrow W$ (750–850 °C). The fourth peak at high temperature (>900 °C) was related to the reduction of $WO_x$ species strongly bounded to $ZrO_2$ support, which contained unreactive oxygen linkage with $ZrO_2$. Similar trend has been observed in our case. The reduction of $WO_x$ species over PtW/Zr catalyst presented four successive peaks centered at 300 °C, 550 °C, 620 °C and 905 °C. Generally, these four peaks moved toward higher temperature with the increase in $SiO_2$ loading owing to the enhanced interaction with support. Specifically, the increase in the fourth reduction peak temperature suggested that the highly dispersed $WO_x$ species exhibited stronger W—O—Zr bond than the bulk ones. As for the second reduction peak, it has been identified to be sensitive to the domain size of $WO_x$ clusters. The bigger the domain size of $WO_x$ clusters was, the higher the ratio of W—O—W linkages and the lower the required reduction temperature were [43]. Thus, the lower second reduction peak temperature of PtW/Zr sample reflected that this sample primarily contained bulk $WO_3$ crystallites. The doping $SiO_2$ into PtW/Zr samples remarkably elevated the reduction temperature, reflecting that more highly dispersed $WO_x$ clusters were formed or even with isolated $WO_x$ species, in well agreement with the XRD, Raman and TEM results.

$NH_3$-TPD technique has been extensively exhibited to probe the amount and strength of acid sites for solid catalysts. The $NH_3$-TPD profiles of $SiO_2$ grafted PtW/Zr catalysts are displayed in Fig. 6. All the samples presented broad $NH_3$-TPD profiles, implying that the surface acid strength was widely distributed on the catalyst surface. Generally, these $NH_3$-TPD peaks can be roughly divided in different strength of acid sites, weak acid sites at ca. 170 °C and medium acid sites at 260 °C, respectively [25]. Apparently, the introduction of $SiO_2$ into PtW/Zr catalyst increased acid amount in terms of weak and medium acid sites. As displayed in Table 1, the total amount of acid sites enhanced gradually with the increasing $SiO_2$ loading, maximized over 5PtW/ZrSi, and then declined slightly. According to previous studies on $WO_x/ZrO_2$ catalysts [27,37], surface polytungstate species were suggested to the sites with strong

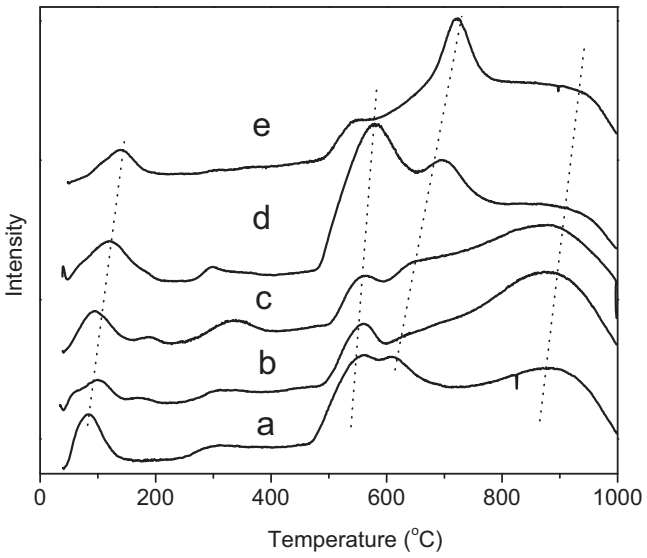


**Fig. 5.** $H_2$-TPR profiles of (a) PtW/Zr, (b) 2.5PtW/ZrSi, (c) 5PtW/ZrSi, (d) 7.5PtW/ZrSi and (e) 10PtW/ZrSi.

acidity while the superfluous tungstate as $WO_3$ crystalline phase did not make contribution to the acid amount. Irrespective of the same $WO_x$ loading, the $SiO_2$ modified catalysts presented more acid amount than PtW/Zr, which can be ascribed to the different surface $WO_x$ states. As revealed by XRD, Raman, TEM and $H_2$-TPR, $WO_x$ over PtW/Zr primarily existed as bulk $WO_3$ crystallites while suitable $SiO_2$ modified samples mainly contained polytungstate species, namely highly dispersed $WO_x$ clusters and some isolated $WO_x$ species. Additionally, it has been reported that the acidity of $SiO_2$–$ZrO_2$ mixed oxides was improved in comparison with either component [4,39]. Thus, the combined results contributed to the higher acid sites of $SiO_2$ doped PtW/Zr catalysts.

### 3.1.3. Surface chemical states

XPS analysis was applied to explore surface chemical states after reduction and surface compositions of these catalysts. As shown in Fig. 7A, the Pt 4f doublet overlapped strongly with W 5s in the range of 69–77 eV, and thus the Pt 4f spectrum must be subtracted from

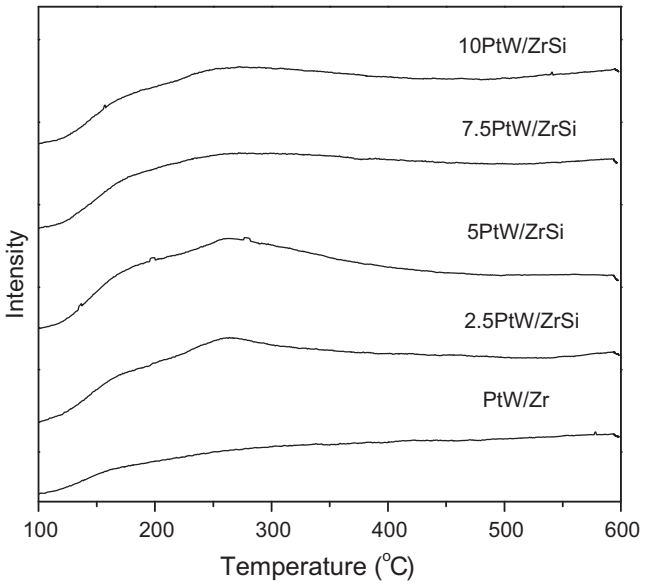


**Fig. 6.** $NH_3$-TPD profiles of $SiO_2$ modified PtW/Zr catalysts.

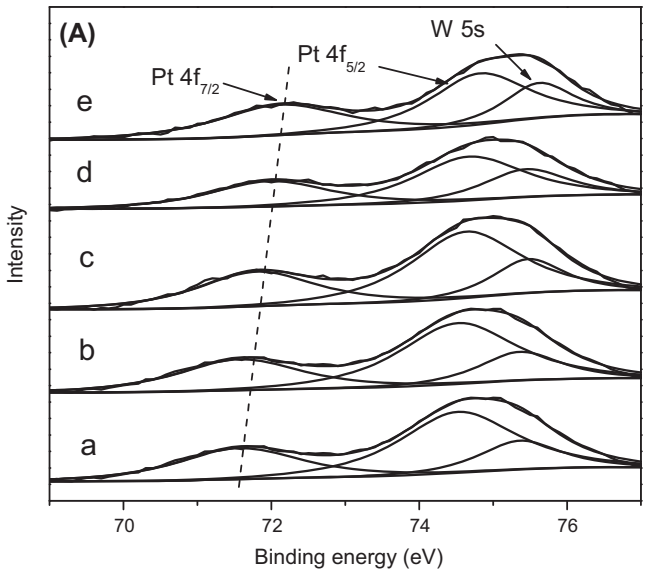


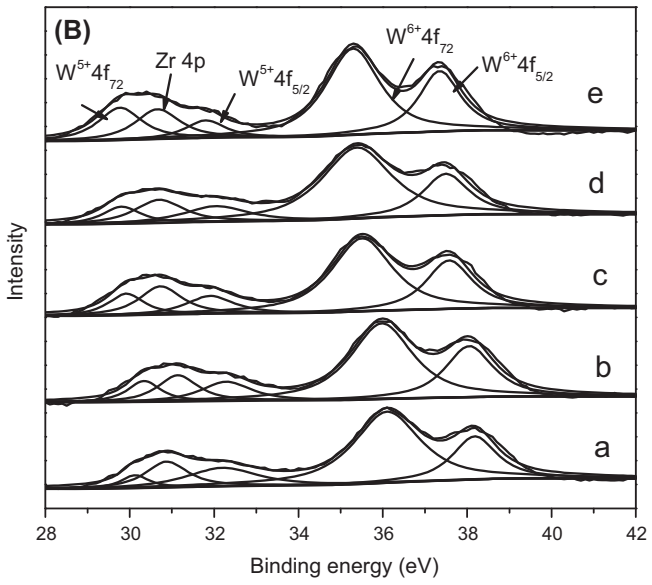


**Fig. 7.** Pt 4f (A) and W 4f (B) XPS photoemission peaks of reduced (a) PtW/Zr (b) 2.5PtW/ZrSi, (c) 5PtW/ZrSi, (d) 7.5PtW/ZrSi and (e) 10PtW/ZrSi catalysts.

the composite signal. The two peaks centered at ca. 71.4 and 74.4 eV were mainly assigned to Pt $4f_{7/2}$ and Pt $4f_{5/2}$ peaks of $Pt^0$, respectively [30]. As listed in Table 2 and Fig. 7A, it should be noted that both of these two peaks shifted toward higher binding energy with increasing $SiO_2$ loading. Meanwhile, the Si 2p and Zr 3d moved toward lower binding energy. This was ascribed to the enhanced electron interaction between Pt and $ZrO_2$ after $SiO_2$ doping. As shown in Table 2, despite the same bulk Pt content, the surface concentration of Pt over PtW/Zr improved obviously owing to $SiO_2$ modification, revealing that the addition of $SiO_2$ apparently elevated Pt dispersion and generated more active sites, consistent well with CO chemisorption and TEM results.

As shown in Fig. 7B, the broad band in the range of 28–42 eV was composed of two doublets of W 4f at different chemical states and Zr 4p component, which was deconvoluted into five peaks. The doublet centered at ca. 30.1 and 32.2 eV were assigned to W $4f_{7/2}$ and W $4f_{5/2}$ of $W^{5+}$ while another one at 35.8 and 38.2 eV were attributed to W $4f_{7/2}$ and W $4f_{5/2}$ of $W^{6+}$ [44]. As shown in Table 2, the ratio of $W^{5+}/(W^{5+}+W^{6+})$ improved with the increasing

**Table 2**
XPS results for $SiO_2$ doped PtW/Zr catalysts.

| Catalyst | Binding energy (eV) | | | | | Surface elemental concentration (at.%) | | $W^{5+}/(W^{5+}+W^{6+})$ |
|---|---|---|---|---|---|---|---|---|
| | Pt $4f_{7/2}$ | $W^{6+}$ $4f_{7/2}$ | $W^{5+}$ $4f_{7/2}$ | Si 2p | Zr 3d | Pt | W | |
| PtW/Zr | 71.4 | 35.8 | 30.1 | – | 182.4 | 0.13 | 1.6 | 0.189 |
| 2.5PtW/ZrSi | 71.5 | 35.6 | 30.3 | 102.5 | 182.3 | 0.16 | 1.7 | 0.202 |
| 5PtW/ZrSi | 71.7 | 35.5 | 29.9 | 102.3 | 182.3 | 0.18 | 1.8 | 0.226 |
| 7.5PtW/ZrSi | 71.8 | 35.4 | 29.8 | 102.1 | 182.3 | 0.16 | 2.1 | 0.196 |
| 10PtW/ZrSi | 72.0 | 35.3 | 29.8 | 102.0 | 182.2 | 0.14 | 2.3 | 0.194 |

$SiO_2$ loading and maximized at 5PtW/ZrSi, revealing that the $SiO_2$ modification was helpful for the generation of $W^{5+}$ with distorted octahedral environment and more structure defects, which may stemmed from the increased $WO_x$–$ZrO_2$ interaction. Additionally, the $SiO_2$ incorporation also enhanced the surface W element concentration, providing clear evidence that the addition of $SiO_2$ tended to disperse $WO_x$ nanoparticles and formed large amount of small clusters and isolated $WO_x$ species.

### 3.2. Catalytic performance of the catalysts

Glycerol hydrogenolysis contained several sequential hydrogenolysis reactions and C—C bonds cleavage reactions, thus it is a challenge to control the product distribution, particularly for obtaining 1,3-PDO selectively. The catalytic performance of glycerol hydrogenolysis over PtW/Zr catalysts with various $SiO_2$ loading was exhibited in a continuous fixed-bed reactor at 180 °C and 5.0 MPa. As listed in Table 3, all the PtW/Zr catalysts containing $SiO_2$ dopants presented higher conversion and 1,3-PDO selectivity than that of unmodified sample. Among them, the 5PtW/ZrSi catalyst reached the excellent performance, 54.3% glycerol conversion with 52.0% selectivity, which appeared to be more superior to the previous Pt–Re/C [45], Rh–Re/$SiO_2$ [46], Pt/$WO_3$/$TiO_2$/$SiO_2$ [22], Pt–$H_4SiW_{12}O_{40}$/$ZrO_2$ [25], Ru/C + $H_2WO_4$ [47]. However, the excessive introduction of $SiO_2$ into PtW/Zr catalyst led to obvious decline of glycerol conversion and 1,3-PDO selectivity. The decrease of 1,3-PDO selectivity was ascribed to the enhanced by-product 1,2-PDO. Additionally, all catalysts presented high selectivity to 1-PO and 2-PO which were derived from the sequential hydrogenolysis via 1,3-PDO and 1,2-PDO in glycerol hydrogenolysis [48].

Space time yield (STY) was employed to reveal the catalytic efficiency. As shown in Table 3, in comparison with PtW/Zr, all the $SiO_2$-doped samples enhanced STY. Among them, the 5PtW/ZrSi catalyst obtained the best results, up to 0.307 mmol/g/h, two times higher than PtW/Zr. Since product distribution is sensitive to the level of conversion, it is desirable to compare the selectivity of different catalysts at the same conversion [49]. Thus, the glycerol conversion of these five catalysts was fixed at ca. 30% by tuning weight hourly space velocity (WHSV). As summarized in Table 4, the selectivity to 1,3-PDO and 1,2-PDO at the same conversion level over PtW/Zr was 44.3% and 6.0%, respectively. Both 1,3-PDO and 1,2-PDO selectivity improved notably over $SiO_2$-doped samples. The 5PtW/ZrSi achieved the best 1,3-PDO selectivity, as high as 60.8%, which was among the highest reported 1,3-PDO selectivity without using organic solvent. The combined results confirmed that $SiO_2$-doped PtW/Zr catalyst was effective for chemoselective hydrogenolysis of glycerol to 1,3-PDO.

**Table 4**
Product selectivity at ca. 30% glycerol conversion over various catalysts[a].

| Catalysts | Selectivity (%) | | | | |
|---|---|---|---|---|---|
| | 1,3-PDO | 1,2-PDO | 1-PO | 2-PO | Others |
| PtW/Zr | 44.3 | 6.0 | 28.9 | 17.7 | 3.1 |
| 2.5PtW/ZrSi | 52.9 | 11.5 | 26.9 | 5.8 | 2.9 |
| 5PtW/ZrSi | 60.8 | 11.1 | 21.4 | 4.6 | 2.1 |
| 7.5PtW/ZrSi | 54.6 | 14.9 | 22.8 | 5.7 | 2.0 |
| 10PtW/ZrSi | 50.8 | 17.6 | 23.6 | 4.9 | 3.1 |

[a] Reaction conditions: 180 °C, 5.0 MPa, $H_2$/glycerol/$H_2O$ = 82:1:46 (molar ratio), WHSV = 1.0–3.0 $h^{-1}$.

## 4. Discussion

### 4.1. The effect of $SiO_2$ doping on the structure and surface features of PtW/Zr catalysts

As indicated by XRD, Raman, TEM and $H_2$-TPR results, $WO_x$ species of $SiO_2$-free PtW/Zr primarily existed as crystalline $WO_3$ while support $ZrO_2$ was dominantly monoclinic. The doped small amount of $SiO_2$ interacted strongly with $ZrO_2$, formed homogenously mixed $ZrO_2$-$SiO_2$ support, which can be verified by the detectable Si—O—Zr linkages from FTIR. Meanwhile, the BET surface area enhanced greatly and the growth of $ZrO_2$ crystalline particles were retarded due to the strong interaction between $SiO_2$ and $ZrO_2$, which resulted in the formation of large amount of small tetragonal $ZrO_2$ nanoparticles. Obviously, these tetragonal $ZrO_2$ nanoparticles can strengthen the interaction with $WO_x$ species, confine the lateral growth of $WO_x$ clusters and promote their dispersion as well as transformation from crystalline $WO_3$ to polytungstate. With further increase in $SiO_2$ content, tetragonal $ZrO_2$ nanoparticles became small and gradually transformed to amorphous phase. Thus, the interaction between highly dispersed $WO_x$ species and $ZrO_2$ became stronger and further promoted the dispersion of active species, which led to the transformation from polytungstate to monotungstate. On the basis of our results and the literature, a possible schematic model about these catalysts is proposed in Fig. 8.

Song et al. [27] have explored the acidic properties of a series of $WO_x/ZrO_2$ catalysts and suggested that the acid sites enhanced continuously with the increasing $WO_x$ loading and reached maximum at the monolayer coverage. The surface monotungstate species presented low acidity while the polytungstate became dominant at the monolayer $WO_x$ coverage and possessed strong acid sites because of the formation of interconnected $WO_x$ species. When the $WO_x$ loading exceeded the monolayer coverage, the redundant $WO_x$ species existed as crystalline $WO_3$ which made no contribution to the total acidity. It appeared that similar behavior was observed in the case of $SiO_2$ modified PtW/Zr samples. As discussed above, the addition of small amount of $SiO_2$ (<5 wt.%) acted to transform crystalline $WO_3$ to polytungstate and thus amplified the number of acid sites. As shown in Table 1, when $SiO_2$ content was up to 5 wt.%, 5PtW/ZrSi obtained the highest total acidity, indicating that polytungstate became predominant and might reach sub-monolayer $WO_x$ coverage. However, the introduction of excessive $SiO_2$ loading (>5 wt.%) promoted the transformation from polytungstate to monotungstate, which led to the decline of total acidity.

On the basis of CO-chemisorption and TEM results, the addition of $SiO_2$ had great impact on the Pt dispersion, which was

**Table 3**
Catalytic performance of glycerol hydrogenolysis over different catalysts[a].

| Catalysts | STY[b] (mmol/$g_{cat}$/h) | Conversion (%) | Selectivity (%) | | | | |
|---|---|---|---|---|---|---|---|
| | | | 1,3-PDO | 1,2-PDO | 1-PO | 2-PO | Others[c] |
| PtW/Zr | 0.144 | 30.0 | 44.3 | 6.0 | 28.9 | 17.7 | 3.1 |
| 2.5PtW/ZrSi | 0.209 | 41.5 | 46.3 | 9.8 | 35.3 | 5.8 | 2.8 |
| 5PtW/ZrSi | 0.307 | 54.3 | 52.0 | 6.8 | 34.0 | 5.6 | 1.6 |
| 7.5PtW/ZrSi | 0.204 | 40.1 | 46.7 | 12.7 | 32.3 | 5.9 | 2.4 |
| 10PtW/ZrSi | 0.164 | 32.1 | 47.1 | 16.5 | 25.9 | 7.9 | 2.6 |

[a] Reaction conditions: 180 °C, 5.0 MPa, $H_2$/glycerol/$H_2O$ = 82:1:46 (molar ratio), WHSV = 1.0 $h^{-1}$. 1,3-PDO: 1,3-propanediol, 1,2-PDO: 1,2-propanediol, 1-PO: 1-propanol, 2-PO: 2-propanol.
[b] STY of 1,3-PDO is millimoles of formed 1,3-PDO per gram of catalyst and per hour.
[c] Others include ethylene glycol, ethanol, methanol, propane, etc.

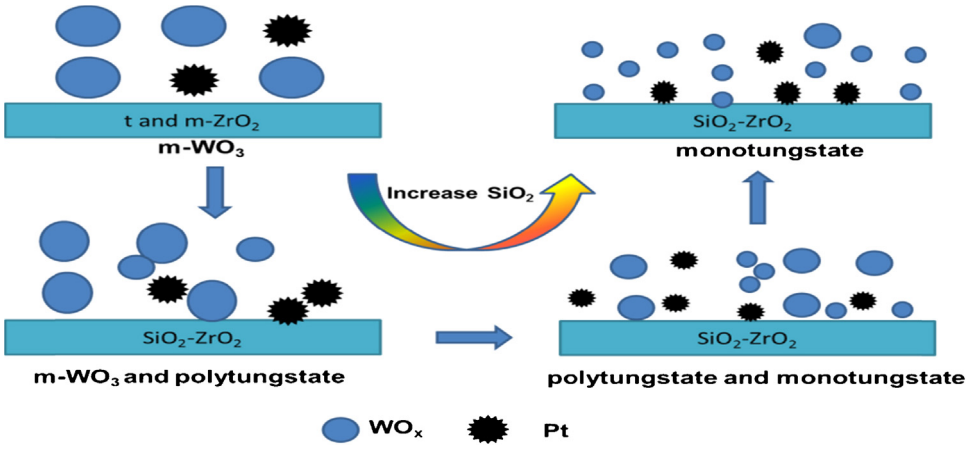


**Fig. 8.** Structure evolution of the PtW/Zr catalysts containing different amounts of $SiO_2$.

illustrated in Fig. 8. Reddy et al. [40] also reported that the $ZrO_2/SiO_2$ mixed support presented higher Rh dispersion than single $ZrO_2$. The strong interaction between $ZrO_2$ and $SiO_2$ was prone to restraining the growth of $ZrO_2$ particles and boosting their dispersion, which enhanced the contact interface between $ZrO_2$ and Pt. The XPS results indicated the improved electronic interaction between $ZrO_2$ and Pt owing to $SiO_2$ modification.

In comparison with monoclinic $ZrO_2$, tetragonal $ZrO_2$ is thermodynamically metastable and inclines to reconstruct to monoclinic $ZrO_2$ upon thermal treatment [50]. It is interesting to find that the tetragonal $ZrO_2$ can be stabilized by introducing small amount of $SiO_2$. The stabilization may be ascribed to the decrease in the coordination number of the $Zr^{4+}$ ion by the incorporation of heterovalent atom. Very recently, Xie et al. [50] have synthesized Na-stabilized tetragonal $ZrO_2$ via hydrothermal method. Compared to monoclinic $ZrO_2$, the tetragonal $ZrO_2$ supported Pt catalyst exhibited much higher Pt dispersion and reaction rate for water gas shift reaction. Thus, the formation of abundant tetragonal $ZrO_2$ stabilized by $SiO_2$ was probably another important reason for elevating Pt dispersion.

### 4.2. The effect of $SiO_2$ doping on the catalytic behavior of PtW/Zr catalysts

Our previous study [24,25] have speculated that the dehydration–hydrogenation mechanism involves in the catalytic process of glycerol hydrogenolysis to 1,3-PDO over metal–acid bifunctional catalysts. The acid sites serve to adsorb glycerol and protonates the secondary hydroxyl group, which will further weaken the secondary C—OH bond and promote its removal as a water molecule. The metal sites serve to dissociatively adsorb $H_2$, provide active atomic hydrogen and undergo hydrogenation of intermediate 3-hydroxypropaldehyde to yield 1,3-PDO. It is well-established that the cooperative effect of active metal and acid sites plays a predominant role in the catalytic performance of glycerol hydrogenolysis and a balanced distribution of metal and acid sites favors to reach outstanding reaction performance [15]. To gain further insight into the structure–activity correlation of these $SiO_2$ modified PtW/Zr catalysts, the effect of $SiO_2$ content on the 1,3-PDO yield as well as Pt dispersion and acidity is illustrated in Fig. 9. The 1,3-PDO yield, Pt dispersion and acidity presented a volcano-type dependence on $SiO_2$ content. Specifically, the 1,3-PDO yield, Pt dispersion and acidity enhanced proportionally with the increase in $SiO_2$ loading up to 5%. Notably, all of them simultaneously reached their summits in the case of 5% $SiO_2$

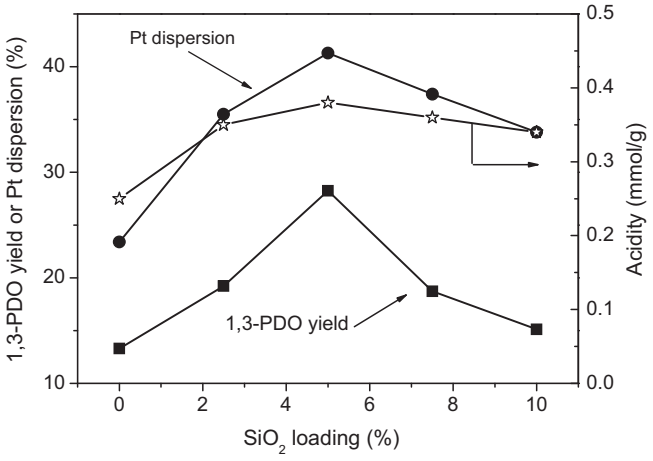


**Fig. 9.** 1,3-PDO yield, Pt dispersion and acidity as a function of $SiO_2$ loading over $SiO_2$ modified PtW/Zr catalysts.

content. After that, all of them decreased gradually. This dependence revealed that both active Pt and acidic sites were essential to achieve superior 1,3-PDO yield. In a word, the above results has confirmed that hydrogenolysis of glycerol to 1,3-PDO conforms to the dehydration–hydrogenation bi-functional mechanism. As discussed above, the polytungstate species contributed to the most acid sites. Accordingly, it is rationally inferred that the Pt and polytungstate species are the dominant active sites for glycerol hydrogenolysis.

The formation of 1,2-PDO proceeds via dehydration of glycerol primary C—OH bond to acetol and consecutive hydrogenation over metal sites [51]. Addition of $SiO_2$ to PtW/Zr modified electronic properties of Pt nanoparticles and resulted in the enhanced 1,2-PDO selectivity. On the other hand, large amounts of 1-PO and 2-PO were produced due to the sequential hydrogenolysis of 1,3-PDO and 1,2-PDO. It is envisaged that designing rational catalyst and optimizing reaction parameters renders it useful in improving 1,3-PDO selectivity at the expense of 1,2-PDO and propanols.

## 5. Conclusions

It has been demonstrated that the addition of $SiO_2$ into $Pt/WO_x/ZrO_2$ played a crucial role in increasing the interaction between active species (Pt and $WO_x$) with support and substantially promoting the dispersion of active species. The introduction of appropriate $SiO_2$ was favorable to the transformation from crystalline $WO_3$ to active polytungstate, while excess $SiO_2$ converted polytungstate to monotungstate. The $SiO_2$ doping remarkably enhanced Pt dispersion and acidity, which led to the improved activity and 1,3-PDO selectivity. The structure-activity correlation revealed that glycerol hydrogenolysis complied with dehydration–hydrogenation reaction mechanism, while Pt and polytungstate had been identified as the dominant active phases.

## Acknowledgment

The authors gratefully acknowledge financial support of the Major State Basic Research Development Program of China (973 Program) (No. 2012CB215305).

## Appendix A. Supplementary data

Supplementary data associated with this article can be found, in the online version, at http://dx.doi.org/10.1016/j.apcatb.2014.04.049.

## References

[1] J.N. Chheda, G.W. Huber, J.A. Dumesic, Angew. Chem. Int. Ed. 46 (2007) 7164.
[2] G.W. Huber, S. Iborra, A. Corma, Chem. Rev. 106 (2006) 4044.
[3] M. Pagliaro, R. Ciriminna, H. Kimura, M. Rossi, C. Della Pina, Angew. Chem. Int. Ed. 46 (2007) 4434.
[4] P. Lauriol-Garbey, S. Loridant, V. Bellière-Baca, P. Rey, J.-M.M. Millet, Catal. Commun. 16 (2011) 170.
[5] I. Gandarias, P.L. Arias, J. Requies, M.B. Guemez, J.L.G. Fierro, Appl. Catal., B: Environ. 97 (2010) 248.
[6] J. Oh, S. Dash, H. Lee, Green Chem. 13 (2011) 2004.
[7] Y. Cui, V. Galvita, L. Rihko-Struckmann, H. Lorenz, K. Sundmacher, Appl. Catal., B: Environ. 90 (2009) 29.
[8] S. Zhu, X. Gao, F. Dong, Y. Zhu, H. Zheng, Y. Li, J. Catal. 306 (2013) 155.
[9] S. Zhu, Y. Zhu, X. Gao, T. Mo, Y. Zhu, Y. Li, Bioresour. Technol. 130 (2013) 45.
[10] S. Hirasawa, H. Watanabe, T. Kizuka, Y. Nakagawa, K. Tomishige, J. Catal. 300 (2013) 205.
[11] S. Zhu, X. Gao, Y. Zhu, Y. Zhu, H. Zheng, Y. Li, J. Catal. 303 (2013) 70.
[12] A. Bienholz, F. Schwab, P. Claus, Green Chem. 12 (2010) 290.
[13] A. Bienholz, H. Hofmann, P. Claus, Appl. Catal., A: Gen. 391 (2011) 153.
[14] I. Jiménez-Morales, F. Vila, R. Mariscal, A. Jiménez-López, Appl. Catal., B: Environ. 117–118 (2012) 253.
[15] S. Zhu, Y. Zhu, S. Hao, L. Chen, B. Zhang, Y. Li, Catal. Lett. 142 (2012) 267.
[16] T. Kurosaka, H. Maruyama, I. Naribayashi, Y. Sasaki, Catal. Commun. 9 (2008) 1360.
[17] M.R. Nimlos, S.J. Blanksby, X. Qian, M.E. Himmel, D.K. Johnson, J. Phys. Chem. A 110 (2006) 6145.
[18] Y. Amada, Y. Shinmi, S. Koso, T. Kubota, Y. Nakagawa, K. Tomishige, Appl. Catal., B: Environ. 105 (2011) 117.
[19] Y. Nakagawa, Y. Shinmi, S. Koso, K. Tomishige, J. Catal. 272 (2010) 191.
[20] J. ten Dam, K. Djanashvili, F. Kapteijn, U. Hanefeld, ChemCatChem 5 (2013) 497.
[21] L.-Z. Qin, M.-J. Song, C.-L. Chen, Green Chem. 12 (2010) 1466.
[22] L. Gong, Y. Lu, Y. Ding, R. Lin, J. Li, W. Dong, T. Wang, W. Chen, Appl. Catal., A: Gen. 390 (2010) 119.
[23] R. Arundhathi, T. Mizugaki, T. Mitsudome, K. Jitsukawa, K. Kaneda, ChemSusChem 6 (2013) 1345.
[24] S. Zhu, X. Gao, Y. Zhu, Y. Zhu, X. Xiang, C. Hu, Y. Li, Appl. Catal., B: Environ. 140–141 (2013) 60.
[25] S. Zhu, Y. Qiu, Y. Zhu, S. Hao, H. Zheng, Y. Li, Catal. Today 212 (2013) 120.
[26] E.I. Ross-Medgaarden, W.V. Knowles, T. Kim, M.S. Wong, W. Zhou, C.J. Kiely, I.E. Wachs, J. Catal. 256 (2008) 108.
[27] K. Song, H. Zhang, Y. Zhang, Y. Tang, K. Tang, J. Catal. 299 (2013) 119.
[28] N. Soultanidis, W. Zhou, A.C. Psarras, A.J. Gonzalez, E.F. Iliopoulou, C.J. Kiely, I.E. Wachs, M.S. Wong, J. Am. Chem. Soc. 132 (2010) 13462.
[29] W. Zhou, E.I. Ross-Medgaarden, W.V. Knowles, M.S. Wong, I.E. Wachs, C.J. Kiely, Nat. Chem. 1 (2009) 722.
[30] Y. Nie, S. Shang, X. Xu, W. Hua, Y. Yue, Z. Gao, Appl. Catal., A: Gen. 433–434 (2012) 69.
[31] M.L. Hernandez-Pichardo, J.A. Montoya de la Fuente, P. Del Angel, A. Vargas, J. Navarrete, I. Hernandez, L. Lartundo, M. González-Brambila, Appl. Catal., A: Gen. 431–432 (2012) 69.
[32] H.-O. Zhu, J.-R. Kim, S.-K. Ihm, Appl. Catal., B: Environ. 86 (2009) 87.
[33] Z. Si, D. Weng, X. Wu, Y. Jiang, B. Wang, Catal. Sci. Technol. 1 (2011) 453.
[34] M.N. Taylor, W. Zhou, T. Garcia, B. Solsona, A.F. Carley, C.J. Kiely, S.H. Taylor, J. Catal. 285 (2012) 103.
[35] B. Katryniok, S. Paul, M. Capron, C. Lancelot, V. Belliere-Baca, P. Rey, F. Dumeignil, Green Chem. 12 (2010) 1922.
[36] L. Han, D. Mao, J. Yu, Q. Guo, G. Lu, Appl. Catal., A: Gen. 454 (2013) 81.
[37] R. Kourieh, S. Bennici, M. Marzo, A. Gervasini, A. Auroux, Catal. Commun. 19 (2012) 119.
[38] G. Cerrato, S. Bordiga, S. Barbera, C. Morterra, Appl. Surf. Sci. 115 (1997) 53.
[39] C. García-Sancho, R. Moreno-Tost, J. Mérida-Robles, J. Santamaría-González, A. Jiménez-López, P. Maireles-Torres, Appl. Catal., A: Gen. 433–434 (2012) 179.
[40] G.K. Reddy, S. Loridant, A. Takahashi, P. Delichère, B.M. Reddy, Appl. Catal., A: Gen. 389 (2010) 92.
[41] T. Ebashi, Y. Ishida, Y. Nakagawa, S.-I. Ito, T. Kubota, K. Tomishige, J. Phys. Chem. C 114 (2010) 6518.
[42] D.G. Barton, S.L. Soled, G.D. Meitzner, G.A. Fuentes, E. Iglesia, J. Catal. 181 (1999) 57.
[43] J.M. Grau, C.R. Vera, V.M. Benitez, J.C. Yori, Energy Fuels 22 (2008) 1680.
[44] M.A. Cortés-Jácome, C. Angeles-Chavez, E. López-Salinas, J. Navarrete, P. Toribio, J.A. Toledo, Appl. Catal., A: Gen. 318 (2007) 178.
[45] O.M. Daniel, A. DeLaRiva, E.L. Kunkes, A.K. Datye, J.A. Dumesic, R.J. Davis, ChemCatChem 2 (2010) 1107.
[46] Y. Shinmi, S. Koso, T. Kubota, Y. Nakagawa, K. Tomishige, Appl. Catal., B: Environ. 94 (2010) 318.
[47] J. Chaminand, L. Djakovitch, P. Gallezot, P. Marion, C. Pinel, C. Rosier, Green Chem. 6 (2004) 359.
[48] S. Zhu, Y. Zhu, S. Hao, H. Zheng, T. Mo, Y. Li, Green Chem. 14 (2012) 2607.
[49] P.T.M. Do, A.J. Foster, J. Chen, R.F. Lobo, Green Chem. 14 (2012) 1388.
[50] H. Xie, J. Lu, M. Shekhar, J.W. Elam, W.N. Delgass, F.H. Ribeiro, E. Weitz, K.R. Poeppelmeier, ACS Catal. 3 (2013) 61.
[51] M.G. Musolino, L.A. Scarpino, F. Mauriello, R. Pietropaolo, ChemSusChem 4 (2011) 1143.